Strain mechanism for order-parameter coupling through successive phase transitions in $PrAlO_3$

Michael A. Carpenter
Department of Earth Sciences, University of Cambridge, Downing Street, Cambridge CB2 3EQ, United Kingdom

Christopher J. Howard
School of Physics, University of Sydney, NSW 2006, Australia and Australian Nuclear Science and Technology Organisation, Private Mail Bag 1, Menai, NSW 2234, Australia

Brendan J. Kennedy
The Heavy Metal Research Centre, School of Chemistry, University of Sydney, NSW 2006, Australia

Kevin S. Knight
ISIS Facility, Rutherford Appleton Laboratory, Chilton, Didcot, Oxfordshire OX11 0QX, United Kingdom
(Received 7 February 2005; published 28 July 2005)

High-resolution powder neutron diffraction data have been collected at ~50 temperatures between 4.2 and 300 K for perovskites $Pr_{1-x}La_xAlO_3$ with $x=0$, 0.05, 0.1, and 0.25. Structural and lattice parameter data extracted by Rietveld refinement have then been used to follow details of octahedral tilting and spontaneous strains associated with the sequence of phase transitions $Pm\bar{3}m \leftrightarrow R\bar{3}c \leftrightarrow Imma \leftrightarrow C2/m$. These are interpreted in terms of strain/order parameter coupling using a single Landau free-energy expansion for a $Pm\bar{3}m$ reference structure with two instabilities (R_4^+ and Γ_3^+ active). Data from the literature relating to the $Pm\bar{3}m \leftrightarrow R\bar{3}c$ transition are consistent with second-order character and an extrapolated transition temperature of 1864 ± 31 K. The $R\bar{3}c \leftrightarrow Imma$ transition is first order in character and can be understood as occurring because coupling takes place between tilting and electronic order-parameter components via a common tetragonal strain. Strains for the $Imma \leftrightarrow C2/m$ transition conform closely to the Landau solution for a proper ferroelastic transition with second-order character and low-temperature saturation. The acoustic anomaly reported at 118 K appears to be associated with a metrically tetragonal structure which develops, as an accidental strain degeneracy, at a temperature between ~110 and ~120 K. Differences in saturation temperatures for the order parameters associated with tilting and electronic ordering are probably responsible for small additional anomalies in the evolution of strains below ~110 K.

DOI: 10.1103/PhysRevB.72.024118 PACS number(s): 64.70.Kb, 61.50.Ks, 61.12.Ld

I. INTRODUCTION

Spontaneous strain might provide the driving mechanism for a phase transition or it might occur by coupling with some other driving mechanism. In both cases, the order parameter has an effective interaction length in a crystal which is determined by the length scale of elastic strain fields. As a consequence, critical fluctuations are suppressed, mean-field behavior is enhanced, and purely displacive systems with strain coupling are expected to conform closely to Landau theory. If the role of strain is so pervasive in determining the evolution of systems which undergo a single phase transition, it is likely also to be a dominant mechanism in controlling coupling between order parameters in systems with more than one instability.[1] For the case of phase transitions in perovskites, such coupling might be between cation ordering, electronic ordering, magnetic ordering, octahedral tilting, etc. The corollary of this is that observed variations of spontaneous strains accompanying phase transitions are expected to provide detailed insights into the mechanisms of both individual and coupled transitions. High-resolution neutron powder diffraction now permits strains to be measured with a resolution of ~0.01% or better, and the purpose of the present study was to test a model of order-parameter coupling by a common strain mechanism for the specific case of coupled phase transitions in $PrAlO_3$.

Phase transitions in $PrAlO_3$ have attracted particular interest because they involve the superposition of a classical Jahn-Teller transition on an octahedral tilting system.[2–19] Understanding the precise sequence of transitions from the cubic structure above ~1800 K to a monoclinic structure below 150 K has evolved with the improved instrumentation available. The most recent view[18] is that the sequence is $Pm\bar{3}m \rightarrow R\bar{3}c$ (~1770 K, continuous), $R\bar{3}c \rightarrow Imma$ (205K, discontinuous), $Imma \rightarrow C2/m$ (150 K, continuous). The rhombohedral structure is stabilized by tilting while the orthorhombic and monoclinic structures are stabilized by a combination of tilting and electronic effects.[5,8] There has been a close examination of a variety of curious properties suggestive of an additional phase transition at ~118 K.[5,7,10,11,13,15,16] The essential point in the present context is that all the structural changes are accompanied by lattice relaxations and that these in turn, when examined at sufficiently high resolution, reveal how the crystals evolve across a multicomponent order-parameter space involving three discrete phase transitions.

Neutron powder-diffraction data are analyzed here in terms of the evolution of symmetry-adapted strains for samples with compositions $PrAlO_3$, $Pr_{0.95}La_{0.05}O_3$, $Pr_{0.90}La_{0.10}O_3$, and $Pr_{0.75}La_{0.25}O_3$ (referred to below as Pr_{100}, Pr_{95}, Pr_{90}, and Pr_{75}). $LaAlO_3$ and, indeed, $NdAlO_3$ undergo the same high-temperature $Pm\bar{3}m \rightarrow R\bar{3}c$ tilting transition as $PrAlO_3$ but do not have comparable electronically driven transitions at low temperatures.[9,19] Substitution of La for Pr causes the transition temperatures in $PrAlO_3$ to be lowered and can be used to investigate which aspects of the low-temperature behavior are intrinsic to the interacting strain effects and which could be due to accidental degeneracies.

II. PREDICTED STRAIN RELATIONS

Phase transitions in $PrAlO_3$ are described here using a Landau free-energy expansion which includes the contributions of both high-temperature octahedral tilting and low-temperature electronic ordering. The space groups of $PrAlO_3$ structures are all subgroups of $Pm\bar{3}m$, which is therefore used as the reference state. For octahedral tilting transitions, the active representation is R_4^+ (using the notation of Miller and Love). In the absence of tilting, the electronic transition would cause a change from cubic to tetragonal symmetry.[5,8] It can be shown using the group theory program ISOTROPY (Stokes and Hatch, Brigham Young University) that Γ_3^+ is the only zone center representation which leads to a tetragonal structure and also gives symmetry subgroups *Imma* and $C2/m$ when coupled with R_4^+. By itself, therefore, the Jahn-Teller transition (Γ_3^+ active) would result in a symmetry change $Pm\bar{3}m \rightarrow P4/mmm$ or *Pmmm*. Combining expansions for R_4^+ (e.g., Refs. 8,20) and Γ_3^+ active (e.g., Ref. 21) gives, for the excess free energy,

$$
\begin{aligned}
G = {} & \frac{1}{2}a\Theta_s\left[\coth\left(\frac{\Theta_s}{T}\right) - \coth\left(\frac{\Theta_s}{T_c}\right)\right](q_1^2+q_2^2+q_3^2) + \frac{1}{4}b(q_1^2+q_2^2+q_3^2)^2 + \frac{1}{4}b'(q_1^4+q_2^4+q_3^4) + \lambda_1 e_a(q_1^2+q_2^2+q_3^2) + \lambda_2[e_{tz}(2q_1^2-q_2^2 \\
& - q_3^2) + \sqrt{3}e_{oz}(q_2^2-q_3^2)] + \lambda_3(e_4q_1q_3 + e_5q_1q_2 + e_6q_2q_3) + \frac{1}{2}a_{JT}\Theta_{s,JT}\left[\coth\left(\frac{\Theta_{s,JT}}{T}\right) - \coth\left(\frac{\Theta_{s,JT}}{T_{c,JT}}\right)\right](q_{oz}^2+q_{tz}^2) + \frac{1}{3}u_{JT}(q_{tz}^3 \\
& - 3q_{tz}q_{oz}^2) + \frac{1}{4}b_{JT}(q_{oz}^2+q_{tz}^2)^2 + \lambda_t(q_{oz}e_{oz} - q_{tz}e_{tz}) + \lambda_a e_a(q_{oz}^2+q_{tz}^2) + \lambda_e[q_{tz}(2e_6^2-e_4^2-e_5^2) - \sqrt{3}q_{oz}(e_4^2-e_5^2)] + \frac{1}{4}(C_{11}^o - C_{12}^o)(e_{oz}^2 \\
& + e_{tz}^2) + \frac{1}{6}(C_{11}^o + 2C_{12}^o)e_a^2 + \frac{1}{2}C_{44}^o(e_4^2+e_5^2+e_6^2). \qquad (1)
\end{aligned}
$$

Here q_1, q_2, q_3 are components of the order parameter for tilting. They can be thought of as relating to rotations of the AlO_6 octahedra about reference axes *Z*, *X*, and *Y*, respectively, i.e., $q_1 \propto \phi_Z$, $q_2 \propto \phi_X$, $q_3 \propto \phi_Y$. The total tilt angle $\phi(=\sqrt{\phi_X^2+\phi_Y^2+\phi_Z^2})$ should scale linearly with the scalar order parameter ($\sqrt{q_1^2+q_2^2+q_3^2}$). The order parameter with Γ_3^+ active has two components, q_t and q_o. These are given here as q_{tz}, q_{oz}, with the subscript z added to indicate that they are specified for a unit-cell orientation which has its unique tetragonal axis parallel to *Z*. Saturation effects, as expressed in terms of saturation temperatures, Θ_s and $\Theta_{s,JT}$, are included following the approach of Salje *et al.*[22] C_{11}^o, C_{12}^o, and C_{44}^o are elastic

TABLE I. Properties of selected subgroups of space group $Pm\bar{3}m$ derived by coupling between separate order parameters associated with Γ_3^+ and R_4^+ representations. The orientations are as given in Howard and Stokes,[23] and as used in Carpenter *et al.*[20]

Subgroup	Order-parameter components		Relationships between order-parameter components	Lattice vectors	Origin
	R_4^+	Γ_3^+			
$P4/mmm$	000	$q_{tz}0$		(100),(010),(001)	(000)
Pmmm	000	$q_{tz}q_{oz}$		(100),(010),(001)	(000)
$R\bar{3}c$	$q_1q_2q_3$	00	$q_1=q_2=q_3$	$(\bar{1}10),(0\bar{1}1),(222)$	(000)
$I4/mcm$	q_100	$q_{tz}0$		$(110),(\bar{1}10),(002)$	(000)
Imma	q_10q_3	$q_{tz}q_{oz}$	$q_1=q_3, q_{oz}=\sqrt{3}q_{tz}$	$(011),(200),(01\bar{1})$	(000)
$C2/m$	q_10q_3	$q_{tz}q_{oz}$		$(0\bar{2}0),(200),(011)$	(1/2 1/2 0)

constants of the parent (cubic) phase. Terms describing direct coupling between the order parameters, such as $\lambda[q_{tz}(2q_1^2 - q_2^2 - q_3^2) - \sqrt{3}q_{oz}(q_2^2 - q_3^2)]$, could have been included but the model presented here is based on the assumption that such coupling occurs indirectly by overlap of strains common to both Γ_3^+ and R_4^+ processes. Direct coupling terms are not considered further, therefore.

Of principal interest in the present context are the terms in q and e, which represent coupling between the order-parameter components and strain. These were obtained using the group theory program ISOTROPY. Linear strains e_1, e_2, e_3 (parallel to X, Y, and Z) are given as symmetry-adapted combinations,

$$e_a = (e_1 + e_2 + e_3), \tag{2}$$

$$e_{oz} = (e_1 - e_2), \tag{3}$$

$$e_{tz} = \frac{1}{\sqrt{3}}(2e_3 - e_1 - e_2), \tag{4}$$

where the subscript z has been added to signify that the unique axis for the tetragonal strain, e_{tz}, is parallel to the reference Z axis. For *Imma* and $C2/m$ structures, in which both sets of order-parameter components have nonzero values, it turns out that the important strains are expressed more conveniently as e_{ox} and e_{tx}, where

$$e_{ox} = (e_2 - e_3), \tag{5}$$

$$e_{tx} = \frac{1}{\sqrt{3}}(2e_1 - e_2 - e_3). \tag{6}$$

Here the unique axis of the tetragonal strain is parallel to the reference X axis. Shear strains e_4, e_5, and e_6 lie in the planes YZ, XZ, and XY, respectively.

Table I lists the properties of selected subgroups of $Pm\bar{3}m$ for which R_4^+ and Γ_3^+ are the active representations. The orientation relationships listed in Table I are also illustrated for unit cells of the $I4/mcm$, *Imma*, and $C2/m$ structures in Fig. 1. These orientations are the same as used elsewhere for the formal analysis of tilting transitions[20,23] but differ from those used previously to describe the structural evolution of $PrAlO_3$. The $C2/m$ structure is more conveniently described in terms of an $I2/m$ cell which has the same orientation as the *Imma* cell. Strain/order-parameter relationships for all these structures, as derived from the equilibrium conditions $\partial G/\partial e_i = 0$, are listed in Table II. Definitions of the strains in terms of lattice parameters are also given in Table II.

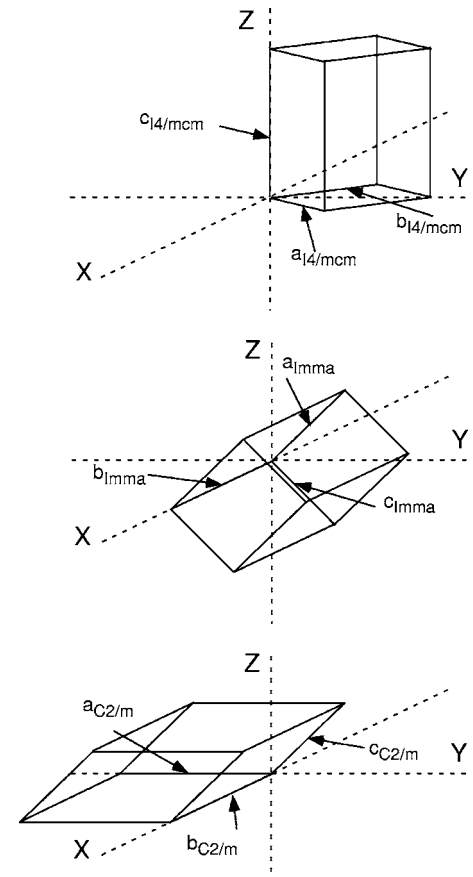

FIG. 1. Relationships between unit-cell orientations for $I4/mcm$, *Imma*, and $C2/m$ structures, as specified by symmetry requirements for phase transitions from a $Pm\bar{3}m$ parent structure. The $I2/m$ structure is in the same orientation as the *Imma* structure, but with $\beta \neq 90°$.

The renormalized form of Eq. (1) obtained by substituting for all strain terms (and assuming $C_{44}^o \gg \lambda_e$) is

$$G = \frac{1}{2}a\Theta_s\left[\coth\left(\frac{\Theta_s}{T}\right) - \coth\left(\frac{\Theta_s}{T_c}\right)\right](q_1^2 + q_2^2 + q_3^2) + \frac{1}{4}b^*(q_1^2 + q_2^2 + q_3^2)^2 + \frac{1}{4}b'^*(q_1^4 + q_2^4 + q_3^4) + \frac{1}{2}a_{JT}\Theta_{s,JT}\left[\coth\left(\frac{\Theta_{s,JT}}{T}\right)\right.$$
$$\left. - \coth\left(\frac{\Theta_{s,JT}}{T^*_{c,JT}}\right)\right](q_{oz}^2 + q_{tz}^2) + \frac{1}{3}u_{JT}(q_{tz}^3 - 3q_{tz}q_{oz}^2) + \frac{1}{4}b_{JT}^*(q_{oz}^2 + q_{tz}^2)^2 - \frac{\lambda_1\lambda_a}{\frac{1}{3}(C_{11}^o + 2C_{12}^o)}(q_1^2 + q_2^2 + q_3^2)(q_{oz}^2 + q_{tz}^2)$$
$$+ \frac{\lambda_2\lambda_t}{\frac{1}{2}(C_{11}^o - C_{12}^o)}[q_{tz}(2q_1^2 - q_2^2 - q_3^2) - \sqrt{3}q_{oz}(q_2^2 - q_3^2)] + \frac{\lambda_3^2\lambda_e}{C_{44}^o}[q_{tz}(2q_2^2q_3^2 - q_1^2q_3^2 - q_1^2q_2^2) - \sqrt{3}q_{oz}(q_1^2q_3^2 - q_1^2q_2^2)], \tag{7}$$

TABLE II. Strain/order-parameter relationships derived from Eq. (1), together with definitions of strain components in terms of the lattice parameter for each structure type; a_o is the unit-cell dimension of the cubic reference structure. The subscript pc is used to signify that the strains for $R\bar{3}c$ are defined using pseudocubic lattice parameters. Note that the expression for e_1, e_2, and e_3 of the $R\bar{3}c$ structure is an approximation which is valid for values of $\propto_{pc}$ that differ only very slightly from 90°. Components q_{tx}, q_{ox} listed here are related to q_{tz}, q_{oz} in Eq. (1) by $q_{tx}=\frac{1}{2}(q_{tz}+\sqrt{3}q_{oz})$, $q_{ox}=\frac{1}{2}(\sqrt{3}q_{tz}-q_{oz})$.

$R\bar{3}c$	*Imma*	*I*2/*m*
$e_a=-3\lambda_1 q_1^2/1/3(C_{11}^o+2C_{12}^o)$	$e_a=(-2\lambda_1 q_1^2-\lambda_a q_{tx}^2)/1/3(C_{11}^o+2C_{12}^o)$	$e_a=(-\lambda_1[q_1^2+q_3^2]-\lambda_a[q_{tx}^2+q_{ox}^2])/1/3(C_{11}^o+2C_{12}^o)$
$e_t=e_o=0$	$e_{tx}=(2\lambda_2 q_1^2-\lambda_t q_{tx})/1/2(C_{11}^o-C_{12}^o)$	$e_{tx}=(\lambda_2[q_1^2+q_3^2]-\lambda_t q_{tx})/1/2(C_{11}^o-C_{12}^o)$
	$e_{ox}=0$	$e_{ox}=(\sqrt{3}\lambda_2[q_1^2-q_3^2]-\lambda_t q_{ox})/1/2(C_{11}^o-C_{12}^o)$
$e_4=e_5=e_6=-\lambda_3 q_1^2/C_{44}^o$	$e_4=-\lambda_3 q_1^2/(C_{44}^o-4\lambda_e q_{tx})$	$e_4=-\lambda_3 q_1 q_3/(C_{44}^o-4\lambda_e q_{tx})$
	$e_5=e_6=0$	$e_5=e_6=0$
$e_1=e_2=e_3=a_{pc}/a_o-1$	$e_1=b/2a_o-1$	$e_1=b/2a_o-1$
	$e_2=e_3=1/2(a/\sqrt{2}a_o+c/\sqrt{2}a_o-2)$	$e_2=1/2((a/\sqrt{2}a_o)(\sin\beta+\cos\beta)+c/\sqrt{2}a_o-2)$
		$e_3=1/2((a/\sqrt{2}a_o)(\sin\beta-\cos\beta)+c/\sqrt{2}a_o-2)$
$e_4=(a_{pc}/a_o)\cos\alpha_{pc}$	$e_4=a/\sqrt{2}a_o-c/\sqrt{2}a_o$	$e_4=(a/\sqrt{2}a_o)\sin\beta-c/\sqrt{2}a_o$

where

$$b^* = b - \frac{2\lambda_1^2}{\frac{1}{3}(C_{11}^o + 2C_{12}^o)} + \frac{4\lambda_2^2}{\frac{1}{2}(C_{11}^o - C_{12}^o)} - \frac{\lambda_3^2}{C_{44}^o}, \tag{8}$$

$$b'^* = b' - \frac{12\lambda_2^2}{\frac{1}{2}(C_{11}^o - C_{12}^o)} + \frac{\lambda_3^2}{C_{44}^o}, \tag{9}$$

$$T_{c,JT}^* = T_{c,JT} + \frac{\lambda_t^2}{a_{JT}\frac{1}{2}(C_{11}^o - C_{12}^o)}, \tag{10}$$

$$b_{JT}^* = b_{JT} - \frac{2\lambda_a^2}{\frac{1}{3}(C_{11}^o + 2C_{12}^o)}. \tag{11}$$

For tilting alone ($q_{tz}=q_{oz}=0$) and assuming that contributions of sixth-order terms in q_1, q_2, q_3 are small, stable products will have $R\bar{3}c$ or $I4/mcm$ symmetry, depending on the actual values of the fourth-order coefficients, b^* and b'^*. The $R\bar{3}c$ form is stable in $PrAlO_3$ and the solution to Eq. (7) for the $Pm\bar{3}m \rightarrow R\bar{3}c$ transition, assuming second-order character, is

$$q_1^2 = \frac{a\Theta_s}{3b^* + b'^*}\left[\coth\left(\frac{\Theta_s}{T_c}\right) - \coth\left(\frac{\Theta_s}{T}\right)\right]. \tag{12}$$

An *Imma* structure would have energies always intermediate between those of the $R\bar{3}c$ and $I4/mcm$ structures and, therefore, would not have an equilibrium stability field.[5,8,24,25] By analogy with the sequence of phase transitions in $BaTiO_3$, which is associated with a single critical temperature, a sequence $Pm\bar{3}m \rightarrow R\bar{3}c \rightarrow Imma \rightarrow I4/mcm$ due to octahedral tilting alone could only be possible if the sixth-order terms were significant and the contribution of fourth-order terms negative[26] (246 potential). For this case, the transitions would all be first order in character.

In the absence of tilting, Eq. (1) would describe a transition from $Pm\bar{3}m$ to $P4/mmm(q_{tz}\neq 0, q_{oz}=0)$ or $Pmmm(q_{tz}\neq 0, q_{oz}\neq 0)$, driven by electronic ordering. In the tilted system, this is modified by coupling between the two sets of order parameters via common strains. Apart from the volume strains, e_a, there are no nonzero strains common to both $P4/mmm$ and $R\bar{3}c$ structures, however. Any effective coupling between the two sets of order-parameter components is therefore restricted to terms in $q_{oz}^2 q_1^2$ and $q_{tz}^2 q_1^2$. On the other hand, there is a tetragonal strain common to both $P4/mmm$ and *Imma* structures that gives rise to coupling terms of the form $q_{tz}q_1^2$ and $q_{oz}q_1^2$. For the orientation relationships in Table II and Fig. 1, this common strain will be e_{tx} and the relevant twin orientation of the $P4/mmm$ structure has its unique tetragonal axis parallel to *X*. Such a twin orientation has

$$q_{tx} = \frac{1}{2}(q_{tz} + \sqrt{3}q_{oz}), \tag{13}$$

$$q_{ox} = \frac{1}{2}(\sqrt{3}q_{tz} - q_{oz}) = 0. \tag{14}$$

The strain e_{tx} due to tilting will act as an applied field for the electronic ordering such that a degree of ordering will be induced above the transition temperature, $T_{c,JT}^*$. For $T_c \gg T_{c,JT}^*$, the Jahn-Teller effects occur in a crystal which has nearly constant tilt angles. In this case the stability of the *Imma* structure can be described by

$$G = \frac{1}{2}a_{JT}\Theta_{s,JT}\left[\coth\left(\frac{\Theta_{s,JT}}{T}\right) - \coth\left(\frac{\Theta_{s,JT}}{T_{c,JT}^*}\right)\right]q_{tx}^2 - \frac{1}{3}u_{JT}q_{tx}^3 + \frac{1}{4}b_{JT}^* q_{tx}^4 - \frac{2\lambda_1\lambda_a}{\frac{1}{3}(C_{11}^o + 2C_{12}^o)}q_{tx}^2 q_1^2 + \frac{2\lambda_2\lambda_t}{\frac{1}{2}(C_{11}^o - C_{12}^o)}q_{tx}q_1^2 - \frac{2\lambda_3^2\lambda_e}{C_{44}^o}q_{tx}q_1^4. \tag{15}$$

At equilibrium, the evolution of q_{tx} in the *Imma* structure is given by

$$\frac{\partial G}{\partial q_{tx}} = 0 = a_{JT}\Theta_{s,JT}\left[\coth\left(\frac{\Theta_{s,JT}}{T}\right) - \coth\left(\frac{\Theta_{s,JT}}{T^{*}_{c,JT}}\right)\right]q_{tx} - u_{JT}q_{tx}^{2} + b^{*}_{JT}q_{tx}^{3} - \frac{4\lambda_1\lambda_a}{\frac{1}{3}(C^{o}_{11}+2C^{o}_{12})}q_{tx}q_1^2 + \frac{2\lambda_2\lambda_t}{\frac{1}{2}(C^{o}_{11}-C^{o}_{12})}q_1^2 - \frac{2\lambda_3^2\lambda_e}{C^{o}_{44}}q_1^4 \quad (16)$$

for which $q_{tx}=0$ is not a solution. Thus, coupling via e_{tx} will stabilize an *Imma* tilt system preferentially to the $R\bar{3}c$ tilt system at all temperatures in the classic manner of behavior induced by an external field.[27] While the *Imma* structure produced by tilting alone cannot be stable with respect to $R\bar{3}c$ in $PrAlO_3$, a first-order transition $R\bar{3}c \rightarrow Imma$ will nevertheless be induced when the additional (negative) energy given by Eq. (15) becomes greater that the free-energy difference between the $R\bar{3}c$ and *Imma* tilted structures.

The $Imma \rightarrow C2/m$ transition is permitted by symmetry to be second order in character. With respect to the cubic reference system used here, the excess free energy for this transition is given by the difference between the excess energy for $Pm\bar{3}m \rightarrow C2/m$, $G_{C2/m}$, and for $Pm\bar{3}m \rightarrow Imma$, G_{Imma}. For a system with a fixed value of the octahedral tilt combination $q_1^2+q_3^2$, this is

$$G_{C2/m} - G_{Imma} = \frac{1}{2}a_{JT}\Theta_{s,JT}\left[\coth\left(\frac{\Theta_{s,JT}}{T}\right) - \coth\left(\frac{\Theta_{s,JT}}{T^{*}_{c,JT}}\right)\right]q_{ox}^2 + u_{JT}q_{tx}q_{ox}^2 + \frac{1}{4}b^{*}_{JT}(q_{ox}^4 + 2q_{tx}^2q_{ox}^2) - \frac{2\lambda_1\lambda_a}{\frac{1}{3}(C^{o}_{11}+2C^{o}_{12})}[q_{ox}^2(q_1^2+q_3^2) - q_{tx}^2(q_1^2-q_3^2)] + \frac{\lambda_2\lambda_t}{\frac{1}{2}(C^{o}_{11}-C^{o}_{12})}(\sqrt{3}q_{ox}-q_{tx})(q_1^2-q_3^2) + \frac{2\lambda_3^2\lambda_e}{C^{o}_{44}}q_{tx}q_1^2(q_1^2-q_3^2). \quad (17)$$

The driving order parameter is q_{ox} and this couples bilinearly with the symmetry-breaking strain, e_{ox}. As required by symmetry, there are no terms which are third order in q_{ox}. The tilt combination $(q_1^2-q_3^2)$ scales as q_{ox} (see Sec. V below), so that the combination $q_{ox}(q_1^2-q_3^2)$ actually behaves as q_{ox}^2. The effect of all the coupling terms which include q_{ox}^2 is to renormalize the transition temperature from $T^{*}_{c,JT}$ to the observed value at $T^{**}_{c,JT}$. A curious feature emerges from the fact that q_{tx} is already nonzero at $T>T^{**}_{c,JT}$. Terms in $q_{tx}(q_1^2-q_3^2)$ and $q_{tx}^2(q_1^2-q_3^2)$ actually behave as $q_{tx}q_{ox}$ and $q_{tx}^2q_{ox}$ with the implication that $q_{tx}\neq 0$ in the *Imma* structure introduces an effective field for the $Imma \rightarrow C2/m$ transition and should cause a tail in q_{ox} above $T^{**}_{c,JT}$. These field terms might be negligible given that q_{tx} is itself likely to be small in the *Imma* structure, which owes its stability, with respect to the cubic parent structure, predominantly to octahedral tilting. In practice, the transition could follow quite closely the solution for a second-order transition comparable in form to Eq. (12).

Within the stability field of the $C2/m$ structure, lattice geometry is determined by the strength of coupling between each of the four order-parameter components $(q_1, q_3, q_{tz}, q_{oz})$ and the strains e_{tx}, e_{ox}, e_a, e_4. The strain e_{ox}, defined with respect to cubic reference axes, becomes $e_5(\sim\cos\beta)$ if reference axes parallel to the crystallographic axes of the *Imma* structure are used. There are insufficient experimental data available to permit calibration of all the coefficients in Eq. (1), but the structural data presented below allow the model to be tested by comparing certain of the observed and predicted strain/strain or strain/order-parameter relationships.

III. EXPERIMENTAL METHODS AND DATA PROCESSING

To prepare the samples of Pr_{100}, Pr_{95}, and Pr_{90}, appropriate stoichiometric amounts of Pr_6O_{11}, La_2O_3, and $Al(NO_3)_3\cdot 9H_2O$ were thoroughly mixed and ground. The material was then transferred to an alumina crucible and heated for 24 h at each of 600, 800, 950, and 1200 °C, the material being reground after each heating step. The material was finally heated at 1200 °C for a further 96 h. Sample purity was monitored using powder x-ray diffraction employing Cu $K\alpha$ radiation. Neutron diffraction patterns showed that small amounts of Al_2O_3 remained as an impurity in the final products. The sample of Pr_{75} was made at a later date, using a slightly different recipe. Al_2O_3 was used as a starting material instead of $Al(NO_3)_3\cdot 9H_2O$. The same final annealing temperature was used but the annealing time was increased, as was the number of regrindings. The final product contained slightly more Al_2O_3 than the other samples, and had somewhat broader powder diffraction peaks.

The neutron diffraction patterns were recorded using the high-resolution powder diffractometer, HRPD, at the ISIS neutron facility, Rutherford Appleton Laboratories (RAL).[28] The same procedure was followed for each of the Pr_{100}, Pr_{95}, and Pr_{90} samples. The powdered sample was lightly packed into an aluminum can of slab geometry, area 20×20 mm, 10 mm thick, with thin neutron-transparent windows front and back. Heat was supplied to the sample through a 100 W cartridge heater inserted in the side wall of the sample can and temperature was monitored through a Rh/Fe sensor located in the opposite wall. A gadolinium, neutron-absorbing mask was attached to the side of the can facing the incident beam and back-scattering detectors to prevent contaminant Bragg peaks arising from either the body of the sample can, including sensor and heater, or the stainless steel frames supporting the vanadium windows. The assembly was attached to a center stick and mounted in an AS Scientific, 50 mm diameter, "Orange" helium cryostat, located at the 1 m position of the diffractometer.[28] The exchange gas was He at 30 mbar. Diffraction patterns were recorded in the back-scattering detector bank over the time-of-flight range 30–130 ms, corresponding to d spacings from 0.6 to 2.6 Å. The instrumental resolution in these patterns is $\delta d/d \approx 4\times 10^{-4}$, independent of d. The patterns were normalized to the incident beam spectrum as recorded in the upstream monitor, and corrected for detector efficiency according to prior cali-

bration with a vanadium scan. After recording a pattern at room temperature, the sample was cooled, then patterns recorded at 4.2 K, at 10 K, then in 10 K steps to 130 K, at 135 K, at 140 K, then in 2 K steps to 160 K, in 5 K steps to 190 K, in 2 K steps to 210 K, and finally in 10 K steps to 300 K. Temperatures were measured and controlled to a precision of about ±0.2 K. The temperatures were chosen, based on previously reported temperatures, in an attempt to provide finer (2 K) steps through the phase transitions. Most patterns were recorded to a total incident proton beam of about 8 μA h, corresponding to approximately 15 min, sufficient to give a good determination of lattice parameters and reasonable estimates of the internal coordinates. At 4.2, 50, 100, 140, 160, and 185 K and at room temperature, longer counting exposures in the range 20–50 μA h were employed, so as to provide a number of superior structure determinations in the temperature ranges of interest. Diffraction patterns were collected at a later date from Pr_{75}. They do not necessarily follow exactly the same temperature scale because of the possibility of drift in the Rh/Fe sensor over the period of 19 months between data collections.

Different phases were identified by close inspection of the diffraction patterns as being consistent with the scheme proposed by Moussa *et al.*[18] These identifications were confirmed, and both lattice parameters and atomic coordinates determined, using the Rietveld method as implemented in the GSAS computer program.[29] The peak shapes were modeled as convolutions of exponential with pseudo-Voigt[29] in which two peak width parameters were varied, and the background as eight-parameter shifted Chebyshev polynomials. Atomic displacement parameters were also refined, though only for the hexagonal structure could the refinement of a full set of anisotropic displacement parameters be supported. The computer program RIETICA[30] was used to check all results. Diffraction patterns from Pr_{75} in the vicinity of the discontinuous $R\bar{3}c \leftrightarrow Imma$ transition showed sufficiently clear evidence of two-phase coexistence that lattice parameters could be obtained for both phases between 160 and 188 K. Certain aspects of the data processing will be explained in greater detail below.

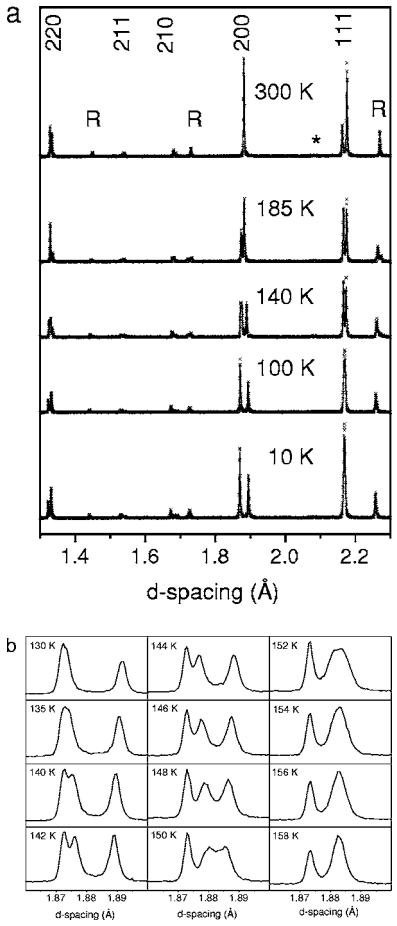

FIG. 2. (a) Segments from diffraction patterns recorded from $PrAlO_3$ at five different temperatures. Crosses indicate the observed data, while the continuous lines are fits obtained by the Rietveld method, assuming structures in $I2/m$ at 10, 100, and 140 K, in *Imma* at 185 K, and in $R\bar{3}c$ at 300 K. Indexing of the main peaks is based on the parent perovskite; the superlattice peaks arising from out-of-phase (R-point) octahedral tilting are also indicated. The asterisk marks a very weak peak from Al_2O_3 impurity. (b) Detail of the splitting of the 200 peak over the temperature range 158–130 K. The peaks index as 040 and 202 in the orthorhombic structure, and the 202 peak, which is broadened above the transition, becomes a $20\bar{2}/202$ doublet in the monoclinic phase.

IV. STRUCTURE ANALYSIS OF $PrAlO_3$

A. Diffraction patterns and structures

Extracts from the diffraction patterns from $PrAlO_3$ recorded at several temperatures (10, 100, 140, 185, and 300 K) are shown in Fig. 2. The main peaks, marked using indices based on the unit cell of the parent cubic structure, show splitting due to the distortion of this "pseudocubic cell."[31] In the pattern recorded at 300 K, the 111 peak shows well resolved splitting to form a doublet with a 1:3 intensity ratio, whereas the 200 peak remains narrow, this being characteristic of patterns from the rhombohedral phase. Comparison of the pattern shown here [Fig. 2(a)] with that in Fig. 4 of Howard, Kennedy, and Chakoumakos[17] shows that much higher resolution has been achieved in the present work. At 185 K, in the orthorhombic phase, the peaks in the 111 doublet have approximately equal intensities, and the 200 peak also splits, giving a doublet with intensity ratio approximately 1:2. Below 150 K, further splitting of peaks can be seen—for example [see Fig. 2(b)], intensity is detached from the longer *d*-spacing side of the 200 doublet and moves to the shorter *d*-spacing side as the temperature is reduced to 140 K. At 100 K, the splitting at 111 is much reduced and the intensities in the 200 doublet reversed (compared with orthorhombic), suggestive of tetragonal symmetry. However, as shown below, tetragonal symmetry is approached, but not achieved, even at 4.2 K. Aside from the peak splitting just discussed, all patterns show superlattice peaks arising from out-of-phase octahedral tilting (*R*-point distortions[23]), characterized by half-integral indices when referred to the pseudocubic cell. Figure 2(a) includes calculated patterns following analysis by the Rietveld method, assuming struc

TABLE III. Details of the structures of $PrAlO_3$ at selected temperatures.

Atom	x	y	z	$U_{iso}(Å^2)\times 10^2$
T=4.2 K, space group $I2/m$, a=5.3189(1), b=7.4797(2), c=5.3299(1)Å, β=90.753(1)°				
Pr	0.2524(14)	0	0.7517(12)	0.42(4)
Al	1/4	1/4	1/4	0.57(5)
O1	0.2177(8)	0	0.2067(8)	0.38(11)
O2	0	0.2904(8)	0	0.98(13)
O3	1/2	0.2588(7)	0	0.71(4)
T=100 K, space group $I2/m$, a=5.3183(1), b=7.4835(2), c=5.3313(1)Å, β=90.703(1)°				
Pr	0.2525(14)	0	0.7507(12)	0.39(4)
Al	1/4	1/4	1/4	0.51(6)
O1	0.2206(9)	0	0.2049(8)	0.51(12)
O2	0	0.2897(8)	0	0.82(13)
O3	1/2	0.2605(7)	0	0.67(5)
T=140 K, space group $I2/m$, a=5.3109(1), b=7.4907(1), c=5.3394(1)Å, β=90.413(1)°				
Pr	0.2498(8)	0	0.7483(6)	0.44(4)
Al	1/4	1/4	1/4	0.53(6)
O1	0.2351(5)	0	0.1979(4)	0.55(6)
O2	0	0.2849(3)	0	0.73(6)
O3	1/2	0.2696(4)	0	0.68(6)
T=185 K, space group $Imma$, a=5.3092(1), b=7.4969(1), c=5.3423(1)Å				
Pr	0	1/4	0.5018(4)	0.55(4)
Al	0	0	0	0.57(5)
O1	0	1/4	0.0527(3)	0.57(4)
O2	1/4	−0.0277(1)	1/4	0.83(3)
T=300 K, space group $R\bar{3}c$, a=5.33375(2), c=12.9773(1)Å				
Pr	0	0	1/4	0.70(3)
Al	0	0	0	0.70(4)
O	0.5428(1)	0	1/4	0.91(2)

tures in $I2/m$, $Imma$, or $R\bar{3}c$ as appropriate. Details of these structures at selected temperatures are reported in Table III.

B. Lattice parameters

The Rietveld method was used to fit all patterns from $PrAlO_3$, assuming initially the structures in $I2/m$ from 4.2 K to 165 K, in $Imma$ from 170 to 210 K, and in $R\bar{3}c$ from 220 K to room temperature. Precise lattice parameters were obtained in every case. However, the refinements did not give a direct measure of the temperature of the continuous transition from $I2/m$ to $Imma$, because the monoclinic phase provided a better fit to the broadened peaks [evident in Fig. 2(b)] to temperatures well above the transition. This might be the tail above $T^{**}_{c,JT}$ predicted by Eq. (17), or it might be a classical effect of susceptibility (as discussed in the following section). However, based on fitting the temperature variation of the angle β and by examining inflections evident in the temperature variation of other lattice parameters, we have estimated the temperature of the transition to be 151.3 K (see Sec. V, below). The analysis was therefore completed assuming $I2/m$ to 150 K, and then $Imma$. Figure 3 shows the temperature dependence of the lattice parameters obtained in the final analysis, along with the cube root of the unit-cell volume, suitably scaled. Inflections in lattice parameters evident at around 150 K were similarly evident in the initial refinements (that is assuming $I2/m$ to 165 K) and are thus not artefacts associated with the (assumed) change in space-group symmetry. Lattice parameters for Pr_{95}, Pr_{90}, and Pr_{75} were obtained in a similar way.

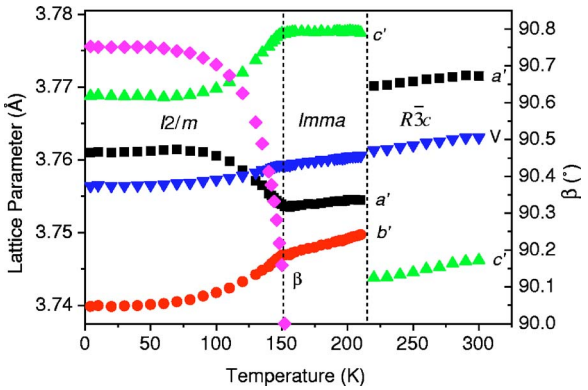

FIG. 3. (Color online) Lattice parameters for $PrAlO_3$, suitably scaled, as a function of temperature. The a', b', c' parameters plotted here are related to the lattice parameters by $a'=a/\sqrt{2}$, $b'=b/2$, $c'=c/\sqrt{2}$ in the $I2/m$ and $Imma$ structures, and $a'=a/\sqrt{2}$, $c'=c/\sqrt{12}$ in $R\bar{3}c$. The cube root of the volume per formula unit is also shown.

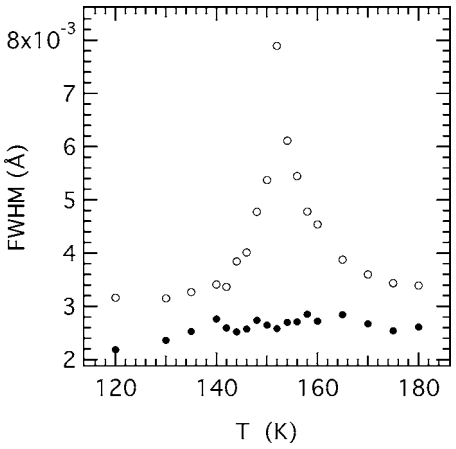

FIG. 4. Widths of selected diffraction peaks as a function of temperature. The narrower peak is from the 040 reflection (orthorhombic indexing); the wider peak is from the orthorhombic 202 reflection above the transition and from each of the $20\bar{2}/202$ doublets below it. The peaks themselves are shown in Fig. 2(b).

C. Peak broadening

Diffraction peak broadening, noted in the previous paragraph and evident in Fig. 2(b), provides further evidence on the nature of the $Imma \leftrightarrow I2/m$ transition. In a proper ferroelastic transition, reflections which are split in diffraction patterns from the low-symmetry phase but merge in diffraction patterns from the high-symmetry phase can show broadening which reflects the susceptibility, χ, of the order parameter. The behavior of As_2O_5 in this regard[32] provides a convenient analogy for understanding the line broadening observed here. Defining the intrinsic linewidth due to the sample as Γ, the evolution of the 202 reflection (splits into $20\bar{2}$ and 202 below T_c) is expected to follow:

$$\Gamma \propto \chi \propto |T - T_c|^{-\gamma} \tag{18}$$

with $\gamma = 1$ for a Landau second-order transition. Γ is thus expected to increase as T_c is approached from above or below and is expected to display a singularity at $T = T_c$. This peak broadening is most conveniently followed by examination of the peaks shown in Fig. 2(b), corresponding to 200 in the cubic perovskite, and indexing as 040 and 202 in the orthorhombic structure. The 040 peak should be unaffected by the transition, but 202 splits in the monoclinic structure into a $20\bar{2}/202$ doublet. The widths of these peaks have been estimated simply from the widths of fitted pseudo-Voigt functions, two such functions being used to fit the orthorhombic 040/202 pair at 152 K and above, and three for the monoclinic at lower temperatures. In the latter case, the widths of the $20\bar{2}$ and 202 peaks were constrained to be equal. The results are shown in Fig. 4. Whereas the width of 040 is essentially constant though the transition, the widths of the orthorhombic 202 and $20\bar{2}/202$ monoclinic peaks both increase as the transition temperature is approached and give a singularity at ~150 K (compare with Fig. 5 of Ref. 32). Instrumental contributions to the linewidths have not been determined, but this result is consistent with the classical picture of a proper ferroelastic transition which is second order in character.

The $R\bar{3}c \leftrightarrow Imma$ transition is not marked by line broadening so much as by overlapping peaks, implying the coexistence of $R\bar{3}c$ and *Imma* structures over some narrow temperature interval.

D. Octahedral tilting

The Rietveld refinements yielded estimates of the internal atomic coordinates at every temperature. Inspection of Table III indicates which atomic position parameters are variable in each of the different structures. Al remains at the inversion center in all structures (note, however, the origin shift between space groups $I2/m$ and *Imma*), and movements of the Pr atom do not significantly exceed the estimated standard deviations. The main changes are in the positions of the oxygen atoms, associated with different patterns and different degrees of octahedral tilting, and particularly impacting on the Pr-O bond lengths.

In $R\bar{3}c$, the only variable position parameter is x(O), and from this we deduce[17] that the AlO_6 octahedron is tilted around its threefold, [111], axis by an angle ϕ given by

$$\tan \phi = 2[x(\mathrm{O}) - 1/2]\sqrt{3}. \tag{19}$$

All directions are given with respect to the cubic aristotype. In *Imma*, the tilting is around the twofold axis ([011]), and leads to shifts z(O1) of the apical oxygen and y(O2) of the equatorial oxygen atoms. The tilt angle ϕ is estimated from the former by

$$\tan \phi = 2z(\mathrm{O1})\sqrt{2}. \tag{20}$$

(The lattice parameters have been removed from this and subsequent expressions by the use of very good approximations such as $a \approx b/\sqrt{2} \approx c$ and, in $I2/m$, $\beta \approx 90°$.) Were the octahedra to tilt as rigid units, the two shifts would be related by $z(\mathrm{O1}) = -2y(\mathrm{O2})$, and z(O1) in Eq. (20) could be replaced by $-2y$(O2). It can be seen from the entry under *Imma* in Table III, as well as from our other data, that this condition is satisfied to a sensible approximation, and we have used the average of z(O1) and $-2y$(O2) in the above equation to obtain our estimates of tilt. Were the octahedra to tilt rigidly about [011] (a axis in *Imma*), the dimension along a would be unchanged and the other dimensions shortened on account of the tilting. After scaling as for the plot in Fig. 3, the a parameter would be the largest. This is not the case—evidently octahedral distortion more than compensates for the effects of tilting on the lattice dimensions. There is thus no prospect of estimating tilt angles from lattice parameters.

In $I2/m$, there is tilting about two axes, and the reduction of oxygen coordinates to octahedral tilt angles is correspondingly more difficult. The octahedra tilt about both [010] and [001] directions of the parent perovskite or, in other words, about both the [011] and $[01\bar{1}]$ directions, which are the a and c axes in $I2/m$. The analysis starts with an identification of the oxygen atoms comprising the octahedron centered on the Al atom at 1/4, 1/4, 1/4. The apical oxygens O1 are at x(O1),0,z(O1) (values as in Table III) and 1/2-x(O1),1/2,

1/2-z(O1), and the tilts around the a and c axes might be determined from the departures from 1/4 of z(O1) and x(O1), respectively. Specifically, these tilt angles ϕ_a and ϕ_c might be estimated from

$$\tan \phi_a = 2[1/4 - z(\mathrm{O1})]\sqrt{2} \tag{21}$$

and

$$\tan \phi_c = 2[x(\mathrm{O1}) - 1/4]\sqrt{2}. \tag{22}$$

The equatorial oxygens O2 and O3 are at 0,y(O2),0;1/2, 1/2-y(O2),1/2; 1/2,y(O3),0; 0,1/2-y(O3),1/2. In this case, rigid tilting of the octahedra would lead to

$$y(\mathrm{O3}) - y(\mathrm{O2}) = x(\mathrm{O1}) - 1/4 \tag{23}$$

and

$$y(\mathrm{O2}) + y(\mathrm{O3}) - 1/2 = 1/4 - z(\mathrm{O1}). \tag{24}$$

Since these equalities are seen to hold to a reasonable approximation, we conclude that the distortion associated with octahedral tilting is not excessive, and again we use averages in estimating the tilt angles. The net tilt in $I2/m$ is computed as the vector sum of tilts ϕ_a on the a axis and ϕ_c on the c axis. This is a tilt of magnitude $\phi = \sqrt{\phi_a^2 + \phi_c^2}$ around an axis lying in the a-c plane [(100) in the parent perovskite] making angles $\psi = \tan^{-1}(\phi_c/\phi_a)$ with the a axis ([011]), and $\psi + \pi/4$ with the parent [001]. The results from these analyses of octahedral tilting are presented in Fig. 5. An alternative account of the tilts can be given by resolving into component tilts, ϕ_X, ϕ_Y, ϕ_Z, occurring about [100], [010], and [001] axes, respectively, of the cubic parent structure. For the structures in $I2/m$, the values of ϕ_Y and ϕ_Z are given by $\phi_Y = \phi\cos(\pi/4 - \psi)$ and $\phi_Z = \phi\sin(\pi/4 - \psi)$. The tilt in *Imma* can be similarly resolved, with $\psi = 0$ in this case.

A remarkable feature apparent in Fig. 5(a) is that the octahedral tilt angle ϕ changes very little as the tilt axis switches discontinuously from [111] to [011] through the transition $R\bar{3}c$ to *Imma* and then swings continuously from [011] towards [001] in the $I2/m$ structure [Fig. 5(a)]. Figure 5(a) also shows the (negative of) angle ψ, measuring the movement of the tilt axis away from [011] toward [001]. Were the tilt axis [001], the structure would be tetragonal in $I4/mcm$, but the above analysis shows that $\psi \approx 35°$ at the lowest temperatures, still some 10° short of [001].

The tilt angles, ϕ_Z and ϕ_Y, are expected to scale with the order-parameter components q_1 and q_3. These will be analyzed below in terms of the variations of q_1^2 and q_3^2, so all the tilt angle data are shown together in Figs. 5(b) and 5(c) as ϕ_Z^2 and ϕ_Y^2. ϕ_Z^2 varies linearly with ϕ_Y^2 as they diverge below the $Imma \leftrightarrow C2/m$ transition point but ϕ_Y^2 does not quite reach zero. Figure 5(b) has qualitatively the same form as Fig. 9(a) of Harley *et al.*[5]

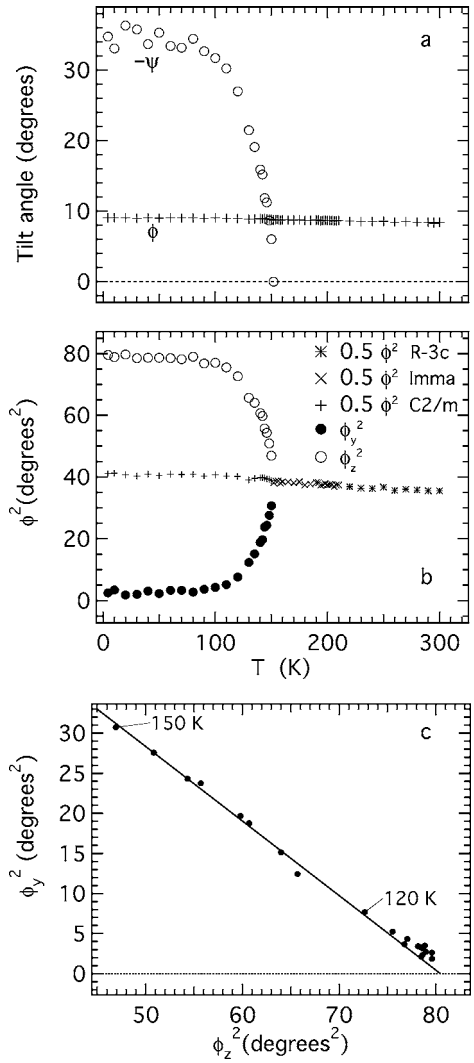

FIG. 5. Variations of octahedral tilt angles. (a) The octahedral tilt angle ϕ appears to vary continuously through the $R\bar{3}c \leftrightarrow Imma$ and $Imma \leftrightarrow C2/m$ transitions. The tilt axis is along [111] from 220 K, along [011] from 170 to 210 K, and below this temperature lies in the (100) plane making an angle $45° + \psi$ with [001]. Though the tilt axis approaches [001], it remains 10° from it at the lowest temperatures. (b) The $Imma \leftrightarrow C2/m$ transition is marked by the divergence of ϕ_Z and ϕ_Y. (c) A straight line fit to the data between 150 and 120 K shows that ϕ_Y^2 varies linearly with ϕ_Z^2 in the $C2/m$ structure.

E. Bond lengths

Electronic effects at low temperatures are expected to be evident from the immediate environment of the Pr^{3+} ion, and in particular from the Pr-O bond lengths. These can be obtained from our results (lattice parameters plus internal coordinates) and are shown, for the temperature range of this study, in Fig. 6. At very high temperatures, in the cubic structure, there are 12 equal Pr-O distances. The equality is broken by octahedral tilting, to give three shorter bonds, six medium bonds, and three longer bonds, at the onset of the transition to the $R\bar{3}c$ structure. This is the coordination at room temperature. There is a further lifting of degeneracies at the transition to the *Imma* phase, where the sets of three bonds split into 1 plus 2, and the set of six into 2 plus 2 plus 2. The end result (Fig. 6) is five distinct Pr-O bond lengths in sets of 1, 4, 2, 4, and 1. In the $C2/m$ phase, eight distinct bond lengths develop, in sets of 1, 2, 1, 2, 2, 1, 2, and 1. At the lowest temperatures, these bond lengths tend to fall into

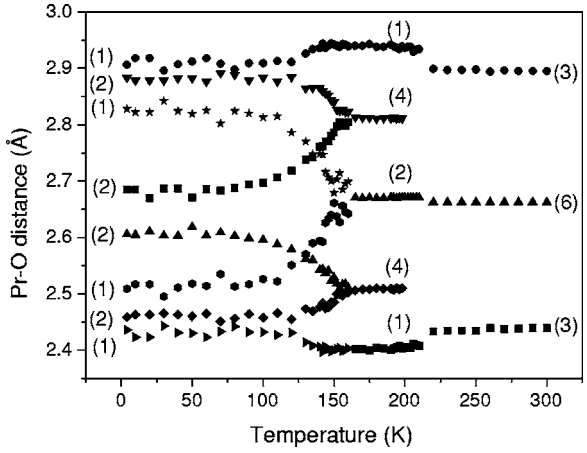

FIG. 6. Temperature variation of the Pr-O bond lengths in $PrAlO_3$. The number in parentheses indicates the number of Pr-O bonds at the indicated length, the total number of Pr-O bonds being 12.

groups: four shorter bonds (1 plus 2 plus 1), four medium bonds (2 plus 2), and four longer bonds (1 plus 2 plus 1). Based on our refinements, we see this tendency for grouping of bond lengths, but we do not yet see just the three distinct bond lengths, four bonds of each length, as would be the case for tetragonal ($I4/mcm$) symmetry.

F. The 118 K anomaly

We conclude this section with a brief comment on the suggestions of an additional 118 K transition, and of tetragonal symmetry at low temperature. For the former, our study might be regarded as the careful neutron diffraction study suggested by Fleury, Lazay, and Van Uitert,[7] but we see nothing unusual in the structural parameters around this temperature (Figs. 3–5). In particular, we have recorded a pattern overnight at 100 K, to a total incident proton beam of 230 μA h, but can discern no evidence in this pattern of any triclinic distortion, such as might be suggested from the EPR data.[15] As regards tetragonal symmetry at low temperature, the unit cell at 4.2 K is very nearly tetragonal, but it can be seen in Fig. 7 that assuming the $I4/mcm$ structure leads to a lower-quality fit to the diffraction pattern recorded.

V. STRAIN ANALYSIS

There are no experimental data for the lattice parameter of cubic $PrAlO_3$ and values of the reference parameter, a_o, for this structure cannot be extrapolated from high temperatures in the usual way. It is necessary, therefore, to resort to the approximation

$$a_o = V^{1/3} = \left(\frac{a_T^2 c_T \sin 2\pi/3}{6} \right)^{1/3}, \tag{25}$$

where a_T and c_T are trigonal unit-cell parameters for the $R\bar{3}c$ structure. Values of the volume strain, e_a, are highly sensitive to the choice of a_o, while values of the shear strains, e_t, e_o, and e_4, are relatively insensitive to this choice.

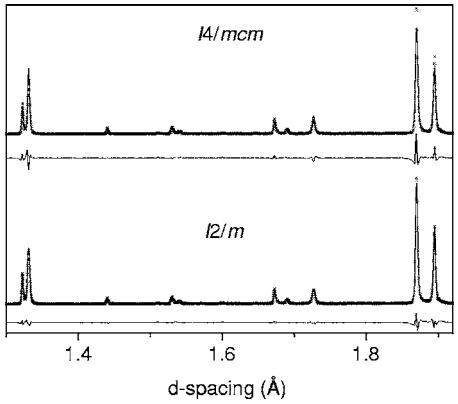

FIG. 7. Comparison of tetragonal ($I/4mcm$) and monoclinic ($I2/m$) models for the structure at low temperature. The figure shows the pattern recorded at 4.2 K (crosses) and the best fit obtained in each case (continuous curve through the pattern). The continuous curve below each pattern represents the difference between the observed pattern and the calculated one. A significantly better fit ($R_{wp}=8.8\%$ cf $R_{wp}=12.2\%$) is obtained from the assumption of monoclinic symmetry.

The baseline parameter, a_o, is itself subject to saturation effects, due to the normal effects of thermal expansion as $T \rightarrow 0$ K. The extrapolation of high-temperature data can be described by a function of the form[22,33,34]

$$a_o = a_1 + a_2 \Theta_{so} \coth\left(\frac{\Theta_{so}}{T} \right), \tag{26}$$

where Θ_{so} is the saturation temperature for the lattice parameter of the $Pm\bar{3}m$ structure. Because of the complication of the additional phase transitions below room temperature, there are insufficient data to constrain a value for Θ_{so} reliably. The same problem does not arise at La-rich compositions in the $(La,Pr)AlO_3$ solid solution, however, and $\Theta_{so} \approx 300$ K provides a reasonable description of the data of Kennedy *et al.*[19] for several samples with different La, Pr contents. This value was adopted to fit the variations of a_o from the high-temperature data for the $R\bar{3}c$ structure of $PrAlO_3$ from Howard, Kennedy, and Chakoumakos,[17] as shown in Fig. 8. There are no equivalent high-temperature data available for Pr_{95}, Pr_{90}, or Pr_{75}. Values for a_2 and Θ_{so} in Eq. (26) were therefore kept at the values obtained for Pr_{100}, and only a_1 was allowed to vary in fitting data for the $R\bar{3}c$ structure of the other samples. The fit parameters obtained were $a_1=3.7462$, 3.7478, 3.7493, and 3.7529Å for Pr_{100}, Pr_{95}, Pr_{90}, and Pr_{75}, respectively (with $a_2=0.000\,043\,24$ Å).

Variations of all the individual and symmetry-adapted spontaneous strains calculated using the expressions given in Table II are shown in Figs. 9 and 10.

A. $Pm\bar{3}m \leftrightarrow R\bar{3}c$ transition

Over a wide temperature interval, e_4 for the $R\bar{3}c$ structure is approximately linear (Fig. 9). A straight line fit to the data above 295 K suggests second-order character for the $Pm\bar{3}m \leftrightarrow R\bar{3}c$ transition, with $T_c=1864\pm31$ K. A small step

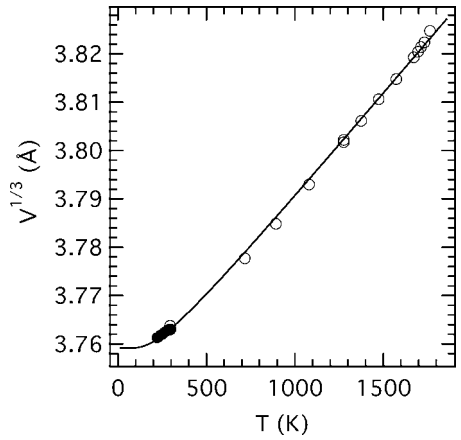

FIG. 8. Data for the cube root of the unit-cell volume of the $R\bar{3}c$ structure of $PrAlO_3$. Open circles denote data from Ref. 17; filled circles denote this study. The curve through the data is a fit using Eq. (26), with Θ_{so} fixed at 300 K.

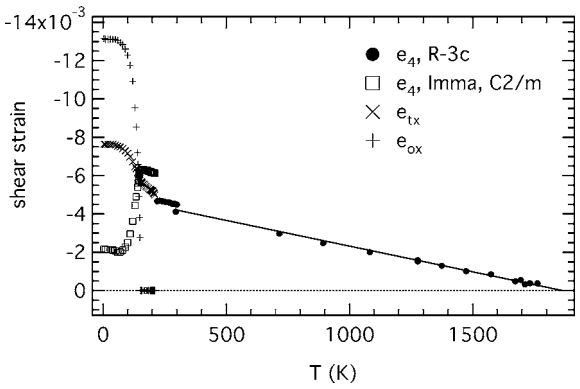

FIG. 9. Shear strains with respect to a cubic reference structure for phase transitions in $PrAlO_3$. Note that the apparent discontinuity in e_4 at 300 K occurs between two different data sets and is not due to a phase transition. The straight line through e_4 data above room temperature represents the standard Landau solution, $e_4 \propto Q^2 \propto (T_c - T)$, for a second-order transition with $T_c = 1864 \pm 31$ K.

in the data at 295 K coincides with a change in the instrument used to collect the data, and presumably arises as a consequence of different calibrations. This does not have a significant impact on our analysis. For the limited range of temperatures over which tilt data are available for the $R\bar{3}c$ structure in the present study, e_4 scales linearly with ϕ^2 [Fig. 11(a)], as expected from the relationship given in Table II.

Because the reference parameter, a_o, was determined using data for the $R\bar{3}c$ structure, it has not been possible to determine the volume strain, e_a, which accompanies the $Pm\bar{3}m \leftrightarrow R\bar{3}c$ transition. A small positive volume strain is observed for the same transition in $LaAlO_3$, however.[34]

B. $R\bar{3}c \leftrightarrow Imma$ transition

The $R\bar{3}c \leftrightarrow Imma$ transition is accompanied by the discontinuous development of a shear strain, e_{tx}; e_4 shows a discontinuity at the transition point but follows a trend in the *Imma* stability field that is parallel to e_4 of the $R\bar{3}c$ structure. A small negative volume strain, e_a, also develops.

If the *Imma* structure is related to the $Pm\bar{3}m$ structure by the same ~1860 K instability that is responsible for the $R\bar{3}c$ structure, both e_{tx} and e_4 would be expected to scale with q_1^2 (Table II). Figure 11(b) shows that e_{tx} varies linearly with e_4 over the short temperature interval of the *Imma* stability field, but the linear fits do not extrapolate to the origin. These

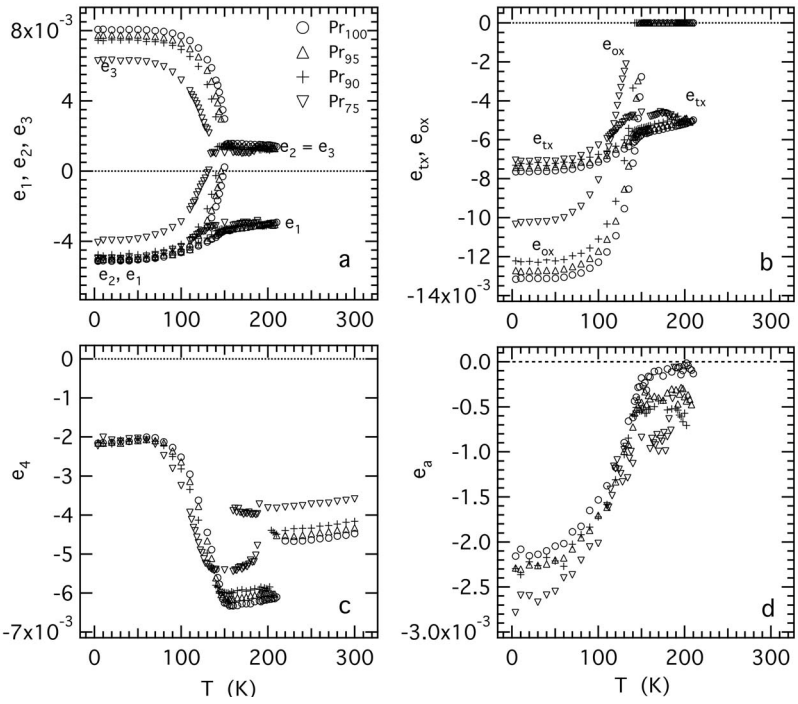

FIG. 10. (a) Expanded view (in comparison with Fig. 9) of linear strains defined with respect to a cubic parent structure. (b) Symmetry-adapted shear strains. The $R\bar{3}c \leftrightarrow Imma$ transition is marked by the discontinuous development of e_{tx}. (c) e_4 shows a break at the $R\bar{3}c \leftrightarrow Imma$ transition but varies continuously through the $Imma \leftrightarrow C2/m$ transition. (d) Volume strain, e_a, defined with respect to the $R\bar{3}c$ structure. A small, negative volume strain accompanies both the $R\bar{3}c \leftrightarrow Imma$ and $Imma \leftrightarrow C2/m$ transitions.

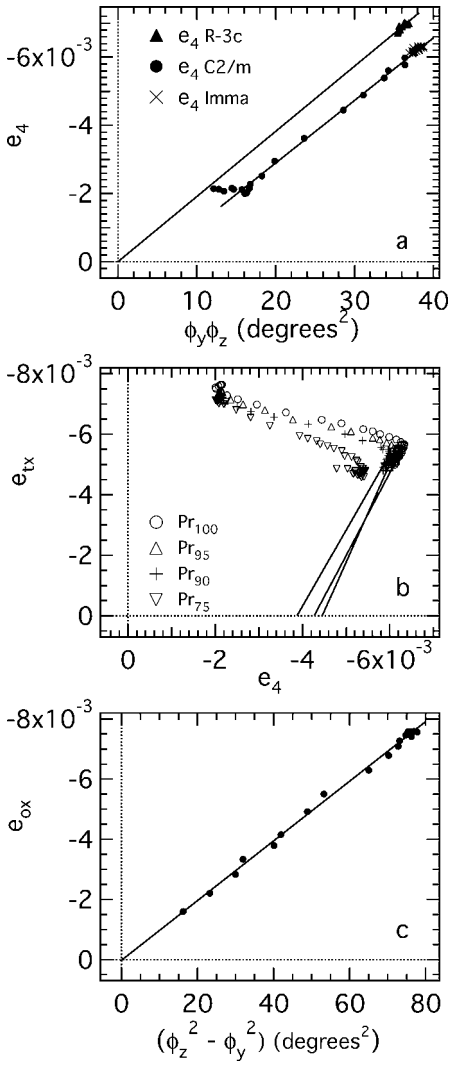

FIG. 11. Strain/tilt and strain/strain relationships. The direction of temperature change is most easily visualized by noting that, with falling temperature, e_4 increases in the $R\bar{3}c$ and *Imma* structures but decreases in the $C2/m$ structure. (a) e_4 is expected to vary linearly with ϕ^2 in the $R\bar{3}c$ structure (straight line passing through the origin), and with $\phi_Y\phi_Z/(C_{44}^o - 4\lambda_e q_{tx})$ in the *Imma* and $C2/m$ structures. The separate trends are consistent with the discontinuous development of q_{tx} at the $R\bar{3}c \leftrightarrow Imma$ transition. (b) The tetragonal strain, e_{tx}, varies linearly with e_4 in the *Imma* stability field, but not in the $C2/m$ field. For *Imma*, both e_{tx} and e_4 are expected to scale with q_1^2 (Table II). The linear fits to *Imma* data shown for Pr_{100}, Pr_{95}, and Pr_{90} do not extrapolate to the origin. (c) e_{ox} is clearly proportional to $(\phi_Z^2 - \phi_Y^2)$.

strains clearly do not evolve as they would be expected to for octahedral tilting associated with a single critical temperature. When plotted against ϕ^2, e_4 shows a break at the $R\bar{3}c \leftrightarrow Imma$ transition that is consistent with the relationship listed in Table II, with the discontinuous development of q_{tx} in the *Imma* structure.

C. $Imma \leftrightarrow C2/m$ transition

Symmetry is broken at the $Imma \leftrightarrow C2/m$ transition by the development of the strain e_{ox}. The transition is also marked by a continuous increase in magnitude of the (negative) strains e_{tx} and e_a, together with a continuous decrease in the magnitude of e_4 [Figs. 10(b) and 10(c)]. As shown in Fig. 11(c), e_{ox} varies linearly with $(\phi_Z^2 - \phi_Y^2) \propto (q_1^2 - q_3^2)$, consistent with $q_{ox} \propto (q_1^2 - q_3^2)$ and the expression for e_{ox} listed in Table II. Figure 12 shows the variations of e_{ox}^2 for each of the four samples. Curves fit to the data are solutions for a second-order transition with the form of Eq. (12), i.e.,

$$q_{ox}^2 \propto e_{ox}^2 \propto \left[\coth\left(\frac{\Theta_{s,JT}}{T_{c,JT}^{**}}\right) - \coth\left(\frac{\Theta_{s,JT}}{T}\right)\right]. \qquad (27)$$

Values of the fit parameters $\Theta_{s,JT}$ and $T_{c,JT}^{**}$ are listed in Table IV. The fits provide reasonable descriptions of the data, and the values of $T_{c,JT}^{**}$, in particular, are tightly constrained. The solution to a 246 Landau potential was also fitted to the data, but this gave values of the Landau c coefficient which were zero within experimental uncertainty limits. Thus the transition appears to be second order in character, with a saturation temperature for the order parameter of ~300 K. This confirms the result of Sturge *et al.*[11] for data collected near $T_{c,JT}^{**}$, but now also explains the nonlinear behavior at lower temperatures as simply the effect of order-parameter saturation.

The observed variation of e_{ox}^2 for Pr_{100} is closely similar to previous measurements of the order-parameter evolution.[8,11,14] In particular, it shows similar small deviations from mean-field evolution in the temperature range ~70–120 K. An equivalent small anomaly is observed also in strain data for the other samples analyzed here, including Pr_{75} (Fig. 12).

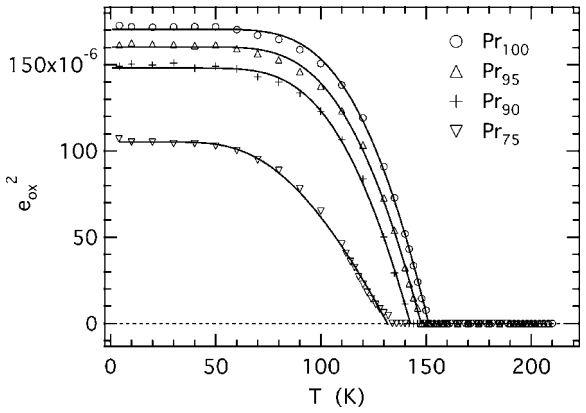

FIG. 12. Fits of Eq. (27) to data for e_{ox}^2 between 4.2 K and just below the $Imma \leftrightarrow C2/m$ transition point. The data are consistent with second-order character for the transition, which occurs at progressively lower temperatures with increasing La content.

TABLE IV. Fit parameters for Eq. (27), as used to describe the variation of e_{ox}^2 for the $C2/m$ structure as a function of temperature.

	Fit range (K)	$T_{c,JT}^{**}$ (K)	$\Theta_{s,JT}$ (K)
Pr_{100}	4.2–150	151.3±0.2	336±7
Pr_{95}	4.2–146	147.6±0.3	312±8
Pr_{90}	4.2–140	142.6±0.4	297±9
Pr_{75}	4.2–132	131.6±0.5	174±7

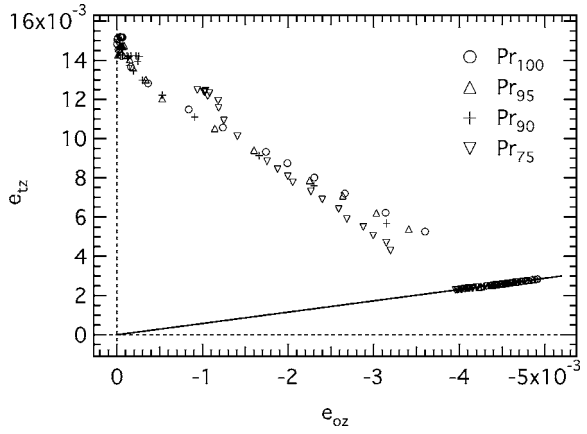

FIG. 13. Variation of the symmetry-breaking strains e_{tz} and e_{oz} within the *Imma* and $C2/m$ structures. (The direction of temperature change is most easily visualized by noting that, with falling temperature, e_{oz} increases in the *Imma* structure but then decreases in the $C2/m$ structure.) By symmetry, the *Imma* structure has $|e_{oz}| \equiv \sqrt{3}|e_{tz}|$ (straight line). A structure with $I4/mcm$ symmetry would have $e_{oz}=0$, $e_{tz}\neq 0$; with falling temperature, the $C2/m$ structure evolves towards this.

D. Strain and the acoustic anomaly at 118 K

If e_{oz} $(=e_1-e_2)$ and e_4, defined with respect to the cubic reference structure, became zero, the symmetry of $PrAlO_3$ would revert to $I4/mcm$ with e_{tz} as the only shear strain. However, while the structure evolves toward this strain state (Fig. 13), e_4 saturates at a value of −0.002 and the tetragonal structure is not achieved [Fig. 10(c)]. There is, nevertheless, a metrically uniaxial structure which is revealed by diagonalizing the strain matrix for strains defined with respect to the cubic reference structure $(e_1,e_2,e_3,e_4,0,0)$. The eigenvalues ε_1, ε_2, ε_3 are principal strains, and the data show that ε_1 and ε_2 converge [Fig. 14(a)], becoming equal at a temperature ~114 K [Figs. 14(b) and 14(c)]. ε_1 is parallel to the X axis of Fig. 1 while ε_2 and ε_3 are in the YZ plane. The axis for ε_3 rotates from parallel to $[0\bar{1}1]$ in the *Imma* stability field toward [001] and levels off at ~5° from [001] below ~80 K [Fig. 14(d)]. This pattern is similar for Pr_{95} and Pr_{90}; $(\varepsilon_1-\varepsilon_2)$ passes through zero at a temperature between ~80 and ~90 K for Pr_{95} but, perhaps, does not quite reach zero in Pr_{90} [Fig. 14(b)]. Neither e_{oz} nor $(\varepsilon_1-\varepsilon_2)$ reaches zero in Pr_{75}.

The temperature at which $(\varepsilon_1-\varepsilon_2)$ passes through zero in $PrAlO_3$ is ~114 K [Fig. 14(c)]. This is, within reasonable experimental uncertainty, the temperature of the "118 K transition." A curious feature of the structural evolution at 118 K is that, apart from the soft acoustic mode observed by Fleury, Lazay, and Van Uitert,[7] any associated changes in other physical properties are only barely detectable. The additional anomalies tend to be small deviations from expected trends in properties which are associated with the $Imma \leftrightarrow C2/m$ transition. For example, Birgeneau *et al.*[8] found a small break in slope of the twin angle as a function of temperature, Sturge *et al.*[11] observed a similar change in the way that the octahedral tilt axis evolves and Harley *et al.*[10] observed a change in the temperature of certain Raman mode frequencies. Fujii, Hidaka, and Wanklyn[16] claimed changes in the temperature dependence of the intensities of selected x-ray diffraction maxima, but Fleury, Lazay, and Van Uitert[7] reported that no excess heat capacity has been detected. There is no other evidence for a symmetry-breaking event and it may be that the acoustic and optic mode softening which occurs as $T\rightarrow 118$ K from above and below is related simply to an accidental strain degeneracy at this temperature. This possibility could be tested by examining the exact orientation of the soft acoustic mode and its symmetry-related equivalents. The unique axis of the uniaxial structure is ~8° from [001] in the YZ plane at 114 K [Fig. 14(d)] and the isotropic section $(\varepsilon_1=\varepsilon_2)$ must, likewise, be tilted out of the XY plane. A degeneracy in acoustic modes would occur in the iso-

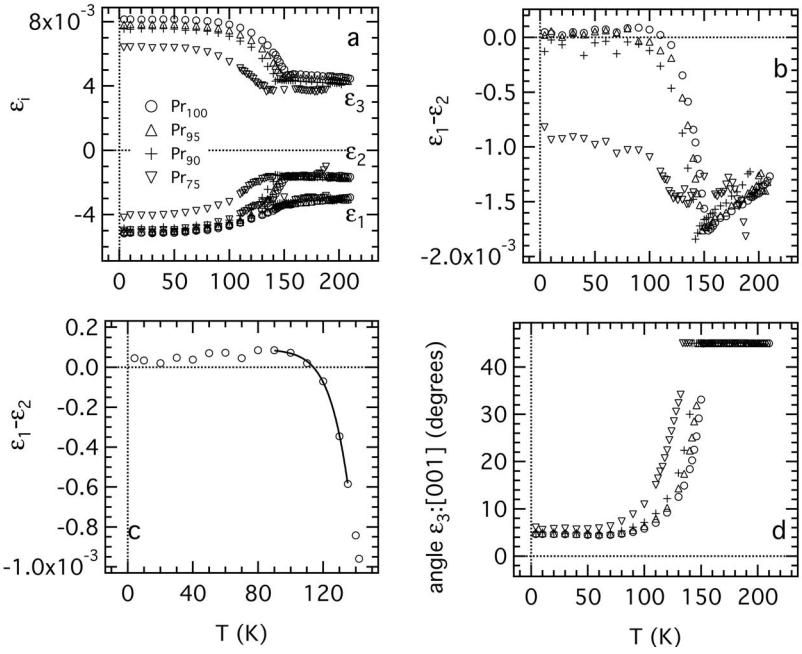

FIG. 14. (a) Values of the principal strains as a function of temperature, obtained by diagonalizing the strain matrix for strains defined with respect to a cubic parent structure. (b) The structure becomes metrically tetragonal when $\varepsilon_1=\varepsilon_2$. (c) Magnified view of data from (b) for $PrAlO_3$. An arbitrary curve through the data shows that a metrically tetragonal state is reached at ~114 K. The pattern of variation of $\varepsilon_1-\varepsilon_2$ below 114 K resembles the pattern of variation shown by an order parameter extracted from EPR data by D'Iorio *et al.* (Ref. 15). (d) ε_3 becomes the unique axis of the metrically tetragonal structure and its orientation lies within the YZ plane (using the reference system shown in Fig. 1). In the $I4/mcm$ structure, ε_3 would be parallel to [001].

tropic strain section so that the propagation direction of the [110] soft mode might actually be displaced by a few degrees towards [001] or [00$\bar{1}$]. When searching for the symmetry-related soft mode, it would be vital to look either just above or just below the *XY* plane, therefore. In this context, it is interesting to note that Fleury, Lazay, and Van Uitert[7] were unable to find a symmetry-related soft mode. Their explanation of this, that $PrAlO_3$ does not have monoclinic symmetry, is not valid in the light of crystallographic studies which have been completed in the intervening years.

Harley[13] and D'Iorio *et al.*[15] developed models which included an additional tilting of the octahedra [out of the (010) plane in their orientation, out of the (100) plane in the orientation used here]. Again, these imply the existence of a small triclinic strain which has not been observed in this study, even in the data set collected at 100 K specifically to look for deviations from monoclinic symmetry. The order parameter evolution given in Fig. 5 of D'Iorio *et al.*[15] actually resembles the variation of $(\varepsilon_1-\varepsilon_2)$ below 114 K [Fig. 14(c)] to a remarkable extent, which raises the question as to whether their ESR results could be explained as being a consequence of the unusual strain evolution.

VI. DISCUSSION

From the perspective of strain alone and using the orientation relationships from Eq. (1), the sequence of phase transitions in $PrAlO_3$ can be described simply as being due to the superposition of successive symmetry-breaking strains, e_4, e_{tx}, and e_{ox}. This contrasts with previous descriptions of a sequence of changing octahedral tilts such that, for the orientation relationships from Eq. (1), a tilt axis of [111] in the $R\bar{3}c$ structure becomes [011] in the *Imma* structure and then rotates away from [011] towards [001] in the $C2/m$ structure. Harley *et al.*[5] and Birgeneau *et al.*[8] recognized that the real behavior of $PrAlO_3$ is determined substantially by coupling of tilting and electronic effects, and this has been formalized here at a macroscopic scale in terms of strain coupling. The two intrinsic instabilities can be understood as becoming three phase transitions due to coupling of each of $q_1(=q_3)$ and q_{tx} to the common tetragonal strain, e_{tx}.

The critical temperatures for tilting and electronic ordering differ by ~1700 K. As a consequence, the Jahn-Teller transition occurs under conditions of almost constant tilt angle, ϕ. Coupling between tilting and the electronic process does cause a small increase in the value of ϕ through each of the low-temperature transitions, however [Fig. 5(b)]. If the volume strain for the $Pm\bar{3}m \rightarrow R\bar{3}c$ transition is positive, as in $LaAlO_3$,[34] overlap with the negative volume strain for $R\bar{3}c \rightarrow Imma$ and $Imma \rightarrow C2/m$ would cause ϕ to decrease. Favorable coupling must be due to overlap of the common shear strain, e_{tx}. On the other hand, from the empirical finding of $q_{ox} \propto (q_1^2-q_3^2)$, it appears that the $Imma \rightarrow C2/m$ transition is driven effectively by the electronic instability alone. The electronic effect imposes a shear strain e_{ox}, which, in turn, imposes the divergence of tilt angles. If there were some driving force from a tilting mechanism with a different critical temperature, the evolution of $\phi_Z^2-\phi_Y^2$ would not follow the simple linear dependence on e_{ox} which is observed.

Previous treatments of the phase transitions in $PrAlO_3$ have not included saturation effects explicitly. Associated with the two sets of order-parameter components are two saturation temperatures, and these need not be the same. Typical values of Θ_s are 0–330 K in other materials, as reported by Hayward and Salje.[35] Some physical insight into the meaning of an observed saturation temperature is obtained by considering coupling between the soft mode for the transition and other hard modes of the material.[35] For example, in the framework silicates, the soft mode might involve rotations of tetrahedra against each other. The tetrahedra are stiff and any vibrations involving tetrahedral distortions will occur at high frequencies and will saturate at relatively high temperatures. Coupling of the soft mode with these will cause the soft mode also to saturate at a relatively high temperature. On the other hand, transitions in perovskites, which typically involve only octahedral rotations, have relatively low values of Θ_s. The $Pm\bar{3}m \leftrightarrow I4/mcm$ transition in $SrTiO_3$ has an order parameter saturation temperature of 90 K (Ref. 35) and the $Pm\bar{3}m \leftrightarrow R\bar{3}c$ transition in $LaAlO_3$ has $\Theta_s = \sim 150$ K.[34] The value of Θ_s for the order parameter of the $Imma \leftrightarrow C2/m$ transition in $PrAlO_3$, at ~300 K, is towards the high end of the scale and presumably arises from the shearing nature of the transition, with distortions of the AlO_6 octahedra being at least as important as their rotations. An independent determination of Θ_s for pure tilting in $PrAlO_3$ cannot easily be made because ϕ is slightly renormalized by coupling with the Jahn-Teller effects. Pérez-Mato and Salje[36] have shown that coupling between processes with different order-parameter saturation temperatures leads to subtle changes in order parameter evolution. The resulting variation of properties which scale with the order parameter, such as strain, then may not quite follow the simplest Landau solution within the saturation regime. It is highly likely that such an effect is responsible for the small but consistent deviations of e_{ox}^2 from a second-order Landau solution (Fig. 12).

In conclusion, the initial premise that strain could be a determinative factor in coupling between two rather different structural instabilities appears to be confirmed for the case of $PrAlO_3$. With the quality of data obtained from high-resolution powder neutron diffraction, it is possible not merely to test details of a mean-field model for the phase transitions but also to identify subtle structural changes recognized also in other types of experiments. All these appear to be understandable from the perspective of strain/order-parameter coupling. The same is likely to be true for other perovskites in which more than one instability can develop.

ACKNOWLEDGMENTS

The neutron facilities at ISIS are operated by the Council for the Central Laboratory of the Research Councils (CCLRC), with a contribution from the Australian Research Council. Travel funding for C.J.H. to ISIS was provided by the Access to Major Research Facilities Program. The studies of perovskites have been partly supported by the Australian Research Council.

[1] E. Salje, Phys. Chem. Miner. **12**, 93 (1985); E. Salje and V. Devarajan, Phase Transitions **6**, 235 (1986).
[2] E. Cohen, L. A. Risberg, W. A. Nordland, R. D. Burbank, R. C. Sherwood, and L. G. Van Uitert, Phys. Rev. **186**, 476 (1969).
[3] R. D. Burbank, J. Appl. Crystallogr. **3**, 112 (1970).
[4] J. K. Kjems, G. Shirane, R. J. Birgeneau, and L. G. Van Uitert, Phys. Rev. Lett. **31**, 1300 (1973).
[5] R. T. Harley, W. Hayes, A. M. Perry, and S. R. P. Smith, J. Phys. C **6**, 2382 (1973).
[6] E. Cohen, M. D. Sturge, R. J. Birgeneau, E. I. Blount, L. G. Van Uitert, and J. K. Kjems, Phys. Rev. Lett. **32**, 232 (1974).
[7] P. A. Fleury, P. D. Lazay, and L. G. Van Uitert, Phys. Rev. Lett. **33**, 492 (1974).
[8] R. J. Birgeneau, J. K. Kjems, G. Shirane, and L. G. Van Uitert, Phys. Rev. B **10**, 2512 (1974).
[9] T. J. Glynn, R. T. Harley, W. Hayes, A. J. Rushworth, and S. H. Smith, J. Phys. C **8**, L126 (1975).
[10] R. T. Harley, W. Hayes, A. M. Perry, and S. R. P. Smith, J. Phys. C **8**, L123 (1975).
[11] M. D. Sturge, E. Cohen, L. G. Van Uitert, and R. P. Van Stapele, Phys. Rev. B **11**, 4768 (1975).
[12] K. B. Lyons, R. J. Birgeneau, E. I. Blount, and L. G. Van Uitert, Phys. Rev. B **11**, 891 (1975).
[13] R. T. Harley, J. Phys. C **10**, L205 (1977).
[14] P. A. Fleury and K. Lyons, Topics in Current Physics **23**, 9 (1981).
[15] M. D'Iorio, W. Berlinger, J. G. Bednorz, and K. A. Müller, J. Phys. C **17**, 2293 (1984).
[16] H. Fujii, M. Hidaka, and B. M. Wanklyn, Phase Transitions **70**, 115 (1999).
[17] C. J. Howard, B. J. Kennedy, and B. C. Chakoumakos, J. Phys.: Condens. Matter **12**, 349 (2000).
[18] S. M. Moussa, B. J. Kennedy, B. A. Hunter, C. J. Howard, and T. Vogt, J. Phys.: Condens. Matter **13**, L203 (2001).
[19] B. J. Kennedy, C. J. Howard, A. K. Prodjosantoso, and B. C. Chakoumakos, Appl. Phys. A **74**, S1660 (2002).
[20] M. A. Carpenter, A. I. Becerro, and F. Seifert, Am. Mineral. **86**, 348 (2001).
[21] M. A. Carpenter and E. K. H. Salje, Eur. J. Mineral. **10**, 693 (1998).
[22] E. K. H. Salje, B. Wruck, and H. Thomas, Z. Phys. B: Condens. Matter **82**, 399 (1991); E. K. H. Salje, B. Wruck, and S. Marais, Ferroelectrics **124**, 185 (1991).
[23] C. J. Howard and H. T. Stokes, Acta Crystallogr., Sect. B: Struct. Sci. **54**, 782 (1988); Acta Crystallogr., Sect. B: Struct. Sci. **58**, 565 (2002).
[24] H. Thomas and K. A. Müller, Phys. Rev. Lett. **21**, 1256 (1968).
[25] C. N. W. Darlington, Phys. Status Solidi B **203**, 73 (1997).
[26] A. F. Devonshire, Philos. Mag. **40**, 1040 (1949); D. Vanderbilt and M. H. Cohen, Phys. Rev. B **63**, 094108 (2001).
[27] A. D. Bruce and R. A. Cowley, *Structural Phase Transitions* (Taylor and Francis, London, 1981); M. A. Carpenter, R. Powell, and E. K. H. Salje, Am. Mineral. **79**, 1053 (1994), and many references therein.
[28] R. M. Ibberson, W. I. F. David, and K. S. Knight, Rutherford Appleton Laboratory Report RAL 92-031 (1992).
[29] A. C. Larson and R. B. Von Dreele, *General Structure Analysis System (GSAS)*, Los Alamos National Laboratory Report LAUR 86-748 (1994).
[30] C. J. Howard and B. A. Hunter, *A Computer Program for Rietveld Analysis of X-ray and Neutron Powder Diffraction Patterns*, Lucas Heights Research Laboratories, New South Wales, Australia (1998), pp. 1–27.
[31] H. D. Megaw, *Crystal Structures: A Working Approach* (Saunders, Philadelphia, 1973), pp. 285–302.
[32] S. A. T. Redfern and E. Salje, J. Phys. C **21**, 277 (1988).
[33] H.-W. Meyer, M. A. Carpenter, A. Graeme-Barber, P. Sondergeld, and W. Schranz, Eur. J. Mineral. **12**, 1139 (2000); H.-W. Meyer, S. Marion, P. Sondergeld, M. A. Carpenter, K. S. Knight, S. A. T. Redfern, and M. T. Dove, Am. Mineral. **86**, 566 (2001); P. Sondergeld, W. Schranz, A. V. Kityk, M. A. Carpenter, and E. Libowitzky, Phase Transitions **71**, 189 (2000); M. A. Carpenter, H.-W. Meyer, P. Sondergeld, S. Marion, and K. S. Knight, Am. Mineral. **88**, 534 (2003).
[34] S. A. Hayward, S. A. T. Redfern, and E. K. H. Salje, J. Phys.: Condens. Matter **14**, 10131 (2002).
[35] S. A. Hayward and E. K. H. Salje, J. Phys.: Condens. Matter **10**, 1421 (1998).
[36] J. M. Pérez-Mato and E. K. H. Salje, Philos. Mag. Lett. **81**, 885 (2001).